remote sensing

MDPI

Article

Exploring Spatial and Temporal Dynamics of Red Sea Air Quality through Multivariate Analysis, Trajectories, and Satellite Observations

Bijoy Mitra [1], Al-Ekram Elahee Hridoy [2], Khaled Mahmud [1], Mohammed Sakib Uddin [1], Abu Talha [3], Nayan Das [4], Sajib Kumar Nath [1], Md Shafiullah [5,6], Syed Masiur Rahman [7] and Muhammad Muhitur Rahman [8,*]

1 Department of Geography and Environmental Studies, University of Chittagong, Chittagong 4331, Bangladesh; bijoymitra11@gmail.com (B.M.); sadman7198@gmail.com (K.M.); sakibges@gmail.com (M.S.U.); kumarnathsajib@gmail.com (S.K.N.)
2 Department of Geography and Environmental Studies, University of New Mexico, Albuquerque, NM 87131, USA; ahridoy@unm.edu
3 Institute of Marine Science, University of Chittagong, Chittagong 4331, Bangladesh; talhacu840@gmail.com
4 Department of Geography, Norwegian University of Science and Technology (NTNU), 7034 Trondheim, Norway; nayand@stud.ntnu.no
5 Control & Instrumentation Engineering Department, King Fahd University of Petroleum & Minerals (KFUPM), Dhahran 31261, Saudi Arabia; shafiullah@kfupm.edu.sa
6 Interdisciplinary Research Center for Sustainable Energy Systems (IRC-SES), King Fahd University of Petroleum & Minerals, Dhahran 31261, Saudi Arabia
7 Applied Research Center for Environment and Marine Studies, Research Institute, King Fahd University of Petroleum & Minerals, Dhahran 31261, Saudi Arabia; smrahman@kfupm.edu.sa
8 Department of Civil and Environmental Engineering, College of Engineering, King Faisal University, Al-Ahsa 31982, Saudi Arabia
* Correspondence: mrahman@kfu.edu.sa

Citation: Mitra, B.; Hridoy, A.-E.E.; Mahmud, K.; Uddin, M.S.; Talha, A.; Das, N.; Nath, S.K.; Shafiullah, M.; Rahman, S.M.; Rahman, M.M. Exploring Spatial and Temporal Dynamics of Red Sea Air Quality through Multivariate Analysis, Trajectories, and Satellite Observations. *Remote Sens.* **2024**, *16*, 381. https://doi.org/10.3390/rs16020381

Academic Editors: Chung-Ru Ho and Carmine Serio

Received: 31 October 2023
Revised: 8 January 2024
Accepted: 12 January 2024
Published: 18 January 2024

Abstract: The Red Sea, a significant ecoregion and vital marine transportation route, has experienced a consistent rise in air pollution in recent years. Hence, it is imperative to assess the spatial and temporal distribution of air quality parameters across the Red Sea and identify temporal trends. This study concentrates on utilizing multiple satellite observations to gather diverse meteorological data and vertical tropospheric columns of aerosols and trace gases, encompassing carbon monoxide (CO), nitrogen dioxide (NO_2), sulfur dioxide (SO_2), and ozone (O_3). Furthermore, the study employs the Hybrid Single-Particle Lagrangian Integrated Trajectory (HYSPLIT) model to analyze the backward trajectory of air mass movement, aiding in the identification of significant sources of air pollutants. A principal component analysis (PCA) with varimax rotation is applied to explore the relationship and co-variance between the aerosol index (AI), trace gas concentrations, and meteorological data. The investigation reveals seasonal and regional patterns in the tropospheric columns of trace gases and AI over the Red Sea. The correlation analysis indicates medium-to-low positive correlations ($0.2 < r < 0.6$) between air pollutants (NO_2, SO_2, and O_3) and meteorological parameters, while negative correlations ($-0.3 < r < -0.7$) are observed between O_3, aerosol index, and wind speed. The results from the HYSPLIT model unveil long-range trajectory patterns. Despite inherent limitations in satellite observations compared to in situ measurements, this study provides an encompassing view of air pollution across the Red Sea, offering valuable insights for future researchers and policymakers.

Keywords: air quality; HYSPLIT model; multivariate analysis; satellite observation; principal component analysis; Red Sea

1. Introduction

Nowadays, maritime transportation is considered the most convenient mode of transport, and its emissions contribute significantly to global air pollution [1,2]. Ship-induced

emissions have increased substantially due to increased international trade [3]. The Intergovernmental Panel on Climate Change (IPCC) addressed the fact that shipping-induced global anthropogenic nitrogen oxide (NO_x = NO + NO_2) and sulfur oxide (SO_x) emissions consist of 15% and 13% of the global emissions, respectively. Moreover, the International Maritime Organization (IMO) has reported that international shipping is estimated to have produced 20.2 million tons of NO_x (as NO_2) and 11.4 million tons of SO_x (as SO_2) in 2018 [4]. In addition, ships at sea emit 5–7 $\times$ 10^9 kg/year of NO_x and 4.7–6.5 $\times$ 10^9 kg/year of SO_2 [5]. It is also estimated that 70% of ship emissions occur within 400 km of land; thus, ships induce air quality degradation in coastal areas and port cities [6]. Furthermore, sulfur from shipping decomposes over the ocean [7] and causes water acidification [8]. CO is emitted from incomplete combustion in ships' diesel engines. Eyring et al. (2005) [9] measured the global annual CO emission from international shipping at 1.31 Tg/year.

The Red Sea, between Asia and Africa, is a vital artery for global trade, with more than 20,000 ships passing through it yearly. Furthermore, world traders use the Red Sea to connect Asia and Europe. Although the Red Sea has been well-known for its untainted water and rich biodiversity over the years, the air quality of the prevailing zone is being contaminated by several anthropogenic activities [10]. The nearby countries of the Red Sea are Yemen, Egypt, Saudi Arabia, and Jordan, which are well known as "oil states" for their vast fossil fuel lifting and refinery industries [11]. As a result, several researchers have evaluated the inconsistent pollution variance in the vicinity of the Red Sea [12–16]. High NO_2 and SO_2 concentrations were recognized near the Red Sea, and the major shipping lanes alongside the Red Sea have been attributed to the emissions from maritime transports [17,18]. Moreover, Alahmadi et al. (2019) [19] quantified the contribution of maritime transport sector emissions to the NO_2 concentration in the Red Sea.

Furthermore, with shipping-induced pollution, on-land gas or oil-powered industries near the sea can substantially source sea air pollutants [20,21]. NO_x is a precursor for surface-level ozone formation, a greenhouse gas contributing to climate warming, forming acidic NO_2 and photochemical smog. Additionally, significant NO_x emissions cause high O_3 concentrations near the Northern Red Sea [22]. However, a few geological phenomena also cause air pollutant transport, e.g., the "jet stream". The earth's rotation causes significant gaseous exchange between air masses.

The geographical location of the Red Sea ranges between 12.5°N and 30°N. In a briefing about the climate of the Red Sea, Pedgley (1974) [23] identified a gap in the upward orography (the physiographic relief of higher elevation) near 19°N, named the Tokar Gap [24]. Here, wind dispersion follows a seasonal contrast as the air stream flows eastward during the summer and westward during the winter [23]. However, with the increase in zonal velocity, air particles' poleward movement breaks down, and they thus shrink near the subtropical zone [25]. Therefore, the spatial location of the Red Sea in the Hadley Cell can be distinguished as a factor in pollutant transport toward the northern region. Moreover, Tadic et al. (2020) [26] demonstrated that the net ozone production rate and precursors are significant near the northern Red Sea. Nevertheless, detailed study of satellite-derived air pollution over the Red Sea is limited. Few in situ studies have been conducted over the Red Sea [17,19,22], but no studies are available on trace gases and their spatial distribution. Therefore, satellite-based remote sensing data can illustrate air pollution over the Red Sea on a large scale where ground-level data are limited [27]. Ground-based observed data might be one of the least affluent methods, but collecting sequential time-series data over the Red Sea is quite capital-intensive and not currently available. Further, satellite data have been widely used to track pollution over maritime regions [28,29]. Although time-series data collection is often limited due to a few natural calamities, satellite-derived data monitor them unceasingly and store them.

In light of the complexities surrounding air quality dynamics over the Red Sea, this study aims, firstly, to comprehensively assess the seasonal and spatiotemporal variations in the vertical tropospheric column concentrations of key air pollutants (e.g., CO, NO_2, SO_2, and O_3) and the aerosol index (AI) using diverse satellite-derived datasets. Secondly, by

employing the Hybrid Single-Particle Lagrangian Integrated Trajectory (HYSPLIT) model, the study seeks to identify significant sources contributing to air pollutant dynamics, providing detailed insights into pollutant transport pathways within the region. Thirdly, the research endeavors to establish correlations between air pollutants and meteorological parameters (AT, SST, SH, WS) to unravel complex relationships. Utilizing a principal component analysis (PCA), the study aims to reveal novel insights into the intricate interplay between pollutants and meteorology. The innovation of this study lies in its multifaceted analysis approach, which elucidates regional patterns in air pollutants and aerosol indices over the Red Sea. By employing advanced analytical techniques, this research significantly contributes to understanding air quality dynamics and pollutant behavior within this critical maritime region.

2. Data and Method

2.1. Study Region

The Red Sea is a semi-encircled tropical basin (Figure 1). It is an inlet of the Indian Ocean between the Saudi Arabian coast and East Africa [30]. Geologically, it is situated at 22°N and 38°E, where the water expands southeast from Suez, Egypt, for about 1200 miles to the Bab el-Mandeb Strait, which connects with the Gulf of Aden and then with the Arabian Sea. The Red Sea is isolated by the Gulf of Aden Strait at Bab al-Mandab in the south, altering the environmental states (e.g., temperature, salinity, shallow depth) and creating a pathway for spreading species [31] between the Red Sea and the Indian Ocean. It separates Egypt, Sudan, and Eritrea to the west from Saudi Arabia and Yemen to the east.

2.2. Methods

The study aims to illustrate the spatiotemporal distribution of the tropospheric column air pollutant data over the Red Sea and its relationship with meteorological parameters. The remotely sensed data (Table 1) were assessed using Google Earth Engine (GEE), and the HYSPLIT model was evaluated on a Windows kernel. The correlation demonstrates the interrelationship among the selected parameters. The multivariate analysis assists in reducing data redundancy, and the back trajectory analysis helps in projecting the transported air mass over the study region.

Table 1. Description of different satellites and data with spatial resolution.

Variable Name	Product Name	Instrument	Spatial Resolution
NO_2	Sentinel-5P NRTI NO_2	TROPOMI Sentinel-5 Precursor	1113.2 m × 1113.2 m
SO_2	Sentinel-5P OFFL SO_2		
O_3	Sentinel-5P OFFL O_3		
CO	Sentinel-5P OFFL CO		
AI	Sentinel-5P OFFL AER AI		
SST	NOAA CDR OISST v2		
AT	NOAA CDR	NOAA	0.05° × 0.05°
WS			
SH			
WV	MERRA-2	GEOS-5	0.5° × 0.625°

2.2.1. Data

Several satellite instruments have been developed to observe gaseous contaminants in the stratosphere and troposphere of the Earth since the first satellite TOMS was launched in 1978 [32]. Copernicus Sentinel-5p contains an advanced air quality monitoring instrument, TROPOMI (Tropospheric Monitoring Instrument), for monitoring the atmosphere and flouting the data gap amongst Envisat satellites [27]. This satellite carries the most advanced TROPOMI instrument for measuring infrared (2305–2385 nm)-to-visible (270–500 nm) spectral bands, which allows it to obtain the concentrations of several ground-level pollutants

more precisely than others [33]. This lets the satellite circle the Earth in one day and finish its orbital cycle in 16 days [34]. Several authors assessed air contaminant data using Sentinel-5p to collect daily time-series data [35–39]. Further, the NOAA Ocean Surface Bundle provides a 3-hourly 0.25 degree resolution grid with high-resolution climatic databases over ice-free ocean surfaces.

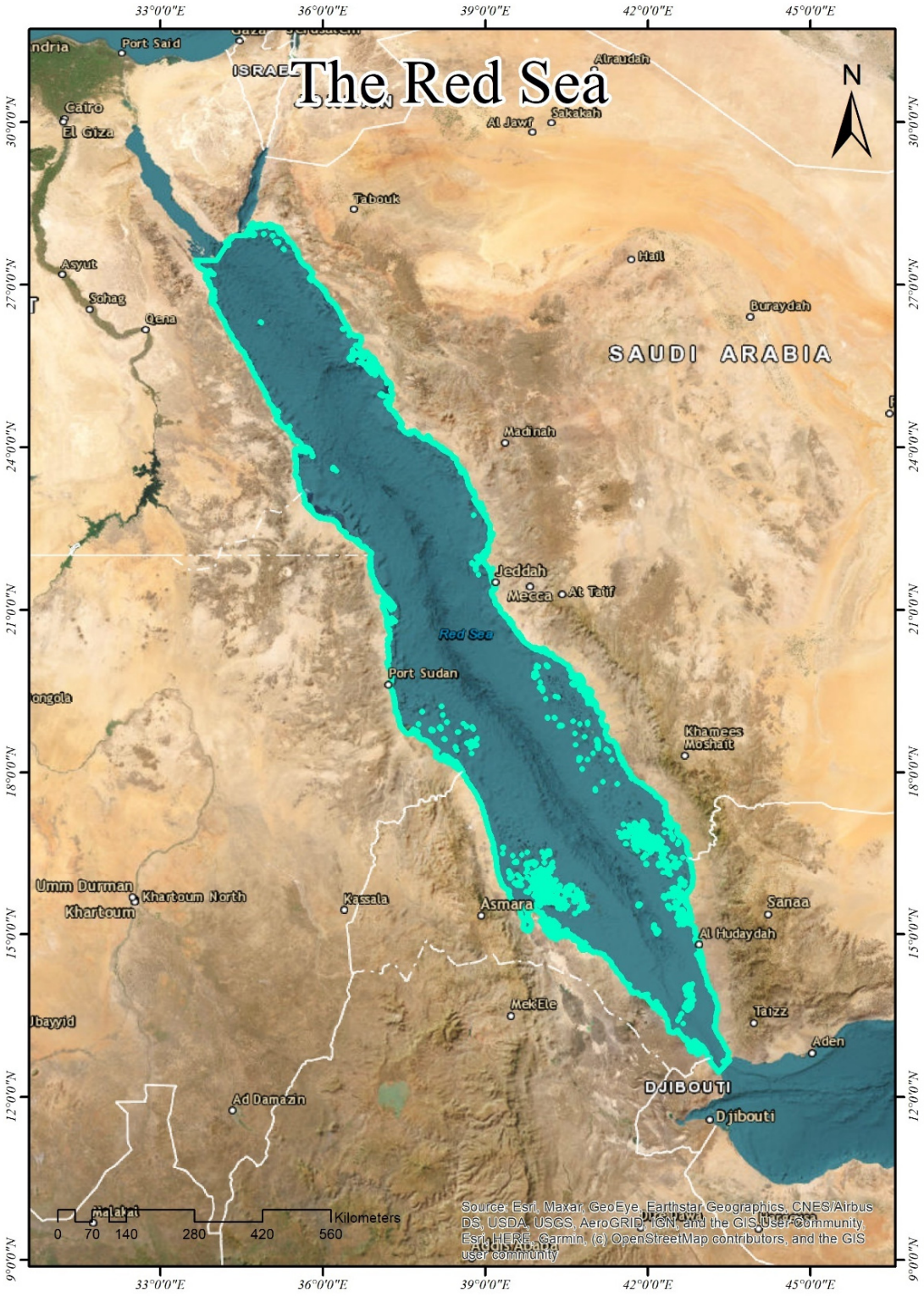

Figure 1. Study region: the Red Sea.

However, for the following study, time-series air pollutants and meteorological parameter data were assessed from Copernicus Sentinel-5p precursor and NOAA Ocean Near-Surface Atmospheric Properties (version 2) using GEE dated from January 2019 to December 2022. The total atmospheric columns of NO_2, SO_2, O_3, CO, and AI were assessed by the GEE code editor to visualize the spatial and temporal air quality dynamics over the Red Sea. Using neural networks, the climatological parameters are assessed based on the solar radiance measurements from the Defense Meteorological Satellite Program (DMSP) spacecraft's Special Sensor Microwave/Imager (SSM/I) and Special Sensor Microwave/Imager Sounder (SSMIS).

To assess the differences among seasonal wind vectors (WVs), the MERRA-2 daily reanalyzed wind vector products (u and v vectors) at 200 hPa have been utilized. This upgraded Goddard Earth Observing System Model, Version 5 (GEOS-5), allows it to model aerosol particles with an improved range of microwave and hyperspectral bands. The average daily vertical (air pollutant and meteorological concentrations) and level 200 hPa products in the troposphere were compared and interpolated on a Python 3.8 medium in the Jupyter Notebook. The spatial resolution of the data products utilized in this study is outlined in Table 1.

2.2.2. Correlation Analysis

A correlation analysis is performed to establish a linear connection between two or more parameters [40]. Pearson's correlation is the most widespread method of correlation analysis, demonstrating a linear correlation between two or more variables and determining and distinguishing a positive or negative correlation [41]. For the following study, Pearson's correlation analysis was performed to determine the relationship between the above meteorological parameters and air pollutants.

2.2.3. Back Trajectory Analysis

The Hybrid Single-Particle Lagrangian Integrated Trajectory (HYSPLIT) model is extensively employed to create air mass backward trajectories in specified starting locations. The model uses meteorological data from the Global Data Assimilation System (GDAS), which are utilized by the Global Forecast System (GFS) model to place observations into a gridded model space to initiate or initialize weather forecasts with observational data [42,43]. This particle trajectory is calculated by taking the standard mean between the 3D velocity vectors for the starting point, $P(t)$, and the first-guess position, $P'(t + dt)$. The velocity vectors are transformed linearly in both time and space.

$$Initial\ Position:\ P'(t+dt) = P(t) + V(P,t)dt \tag{1}$$

$$Final\ Destinantion:\ P(t+dt) = P(t) + 0.5\left[V(p,t) + V\left(P_2^1 t + dt\right)\right]dt \tag{2}$$

From Equations (1) and (2), the trajectories discontinue at the model surface. Advection continues along the ground if the vectors cross. Simulations support varied integrating time steps (dt). The calculation requires that the time-step advection radius not be greater than 0.75 of the meteorological grid frequency.

Since 2011, the National Oceanic and Atmospheric Administration's (NOAA) Air Resources Laboratory (ARL) has been providing GDAS data with a 0.5° horizontal resolution and 55 vertical layers [44]. This allows us to obtain detailed information on the likely dispersal of pollutants from potential samples, allowing us to "attribute" air pollution to specific sources in specific locations [45]. Tian (2020) [46] also illustrated Shenyang City's pollution characteristics using HYSPLIT modeling.

2.2.4. Principal Component Analysis

To reduce the data's dimensions, a principal component analysis was performed. It was introduced by Pearson in 1901. PCA is a widely used method in air pollution studies to decrease the redundancy of the variables. It predicts the directions of the variables

where the data have significant variability [47,48]. The similarity among the PCs can be established based on the influence of different variables. Usually, PCs are explained with the following equation.

$$PC_i = l_{1i}X_1 + l_{2i}X_2 + \ldots\ldots + l_{mi}X_m \quad (3)$$

Here, PC_i is the i^{th} principal component, and X_i is the i^{th} loading of the observed variable.

The PCA is subtracted from the eigenvalues and eigenvectors calculations [49]. Eigenvalues larger than or equal to 1 should be retained for all PCs. A strong factor loading is measured when the FL is greater than 0.75; values ranging from 0.5 to 0.75 are considered moderate; and values below 0.49 are considered weak factor loading [50].

2.2.5. NOAA HYSPLIT Model

The NOAA HYSPLIT model was used to assess backward trajectories to identify the emergence of air masses over the Red Sea. This study calculated the trajectories for 48 h at 500, 1000, and 2000 m (AGL) to understand the complexity of air masses near the surface. Due to the large number of trajectory simulations, the maps retrieved at the two absolute extremes of the seasonal cycle of wind direction in the Red Sea for each study year were used as an example. Therefore, the back trajectories for January, April, July, and October 2019 are shown as references. The starting point for the trajectory clustering is (27.60°N, 34.27°E), updated daily at 00:00, 06:00, 12:00, 18:00, and 24:00 UTC. The red, blue, and green lines represent the paths of air masses at 500 m, 1000 m, and 2500 m AGL (above ground level), respectively.

3. Results and Discussions

3.1. Descriptive Statistics

Table 2 shows a statistical summary of the daily air pollutant concentrations and other meteorological parameters over the Red Sea. It shows that the mean AT and SST were, respectively, 27.9 ± 1.98 °C and 28.4 ± 2.34 °C. However, Shaltout [51] measured the annual mean SST as 27.88 ± 2.14 °C between 1982 and 2016. This denotes a gradual increase in the SST over the Red Sea. Further, the maximum values consist of 31.1 °C and 32.1 °C, and the minimum values are, respectively, 23.4 °C and 22.1 °C. The time-series variation in the SST is greater than that in the AT, as the SST consists of a more significant standard deviation than the AT. Moreover, during the study period, the WS ranged from 8.82 m/s to 2.54 m/s (the mean WS 4.68 ± 1.37 m/s), and the SH ranged between 20.1 g/kg and 12.6 g/kg (the mean SH was 16.9 ± 1.45 g/kg). A positive change can be observed in the SH concentration with an increase in the surrounding temperature.

Table 2. Descriptive statistics of meteorological parameters and tropospheric column air pollutant data.

Statistics	SH (g/kg)	WS (ms^{-1})	AT (°C)	SST (°C)	NO_2 ($\mu molm^{-2}$)	SO_2 ($\mu molm^{-2}$)	O_3 ($\mu molm^{-2}$)	CO ($\mu molm^{-2}$)	AI
Mean	16.9	4.68	27.9	28.4	50.1	195	0.118	31905	−0.699
Standard deviation	1.45	1.37	1.98	2.34	7.32	141	0.00507	3701	0.726
Minimum	12.6	2.54	23.4	22.1	27.8	6.34	0.104	18874	−3.13
Maximum	20.1	8.82	31.1	32.1	70.0	763	0.128	44683	1.96
Skewness	−0.737	0.810	−0.499	−0.363	0.280	1.10	−0.723	0.307	0.951

The average vertical tropospheric column concentration of NO_2 is 50.1 ± 7.32 $\mu molm^{-2}$, with a minimum of 27.8 $\mu molm^{-2}$ and a maximum of 70 $\mu molm^{-2}$. The average column concentration of SO_2 is 195 ± 141 $\mu molm^{-2}$, with maximum and minimum values of, respectively, 763 $\mu molm^{-2}$ and 6.34 $\mu molm^{-2}$. Further, with maximum and minimum values of 44,683 $\mu molm^{-2}$ and 18,874 $\mu molm^{-2}$, the vertically integrated average CO column density was 31,905 ± 3701 $\mu molm^{-2}$. This column also indicates a moderately

high concentration regarding coastal environments [52,53]. The AI ranged from 1.96 to −3.13 (with an average of -0.699 ± 0.726). SO_2 and the AI show strong positive skewness, while NO_2 and CO are moderately positively skewed. Positive skewness refers to the mean concentration of air pollutants being higher than the median. Further, positively skewed distributions refer to naturally stirring phenomena [54]. However, the measured monthly O_3 mean column concentration was 0.118 ± 0.005 µmolm^{-2}. Its standard deviation illustrates very low clustering, and the median value is higher than the mean concentration of O_3.

3.2. Correlation Analysis

To explore the relationship between the air pollutants and meteorological data, Pearson's correlation analysis was employed. NO_2 is positively correlated with AT, SH, and SST (Figure 2). SO_2 shows a moderate ($p < 0.01$) positive correlation with AT (R = 0.155), while O_3 is positively correlated with AT, SH, and SST with higher significant confidence ($p < 0.001$). Here, a positive correlation between the three parameters (AT, SH, and SST) is expected since they are distinguished forces of O_3 dynamics. However, a negative correlation (R = −0.44) between O_3 and WS was found. A higher wind speed dilutes or disperses emissions, reducing O_3 formation [55]. A negative correlation between O_3 and WS was also found by [55,56]. Further, CO is negatively correlated with all the parameters except WS (R = 0.296). The AI is positively correlated with SH, SST, NO_2, and O_3 and negatively correlated with WS and NO_2.

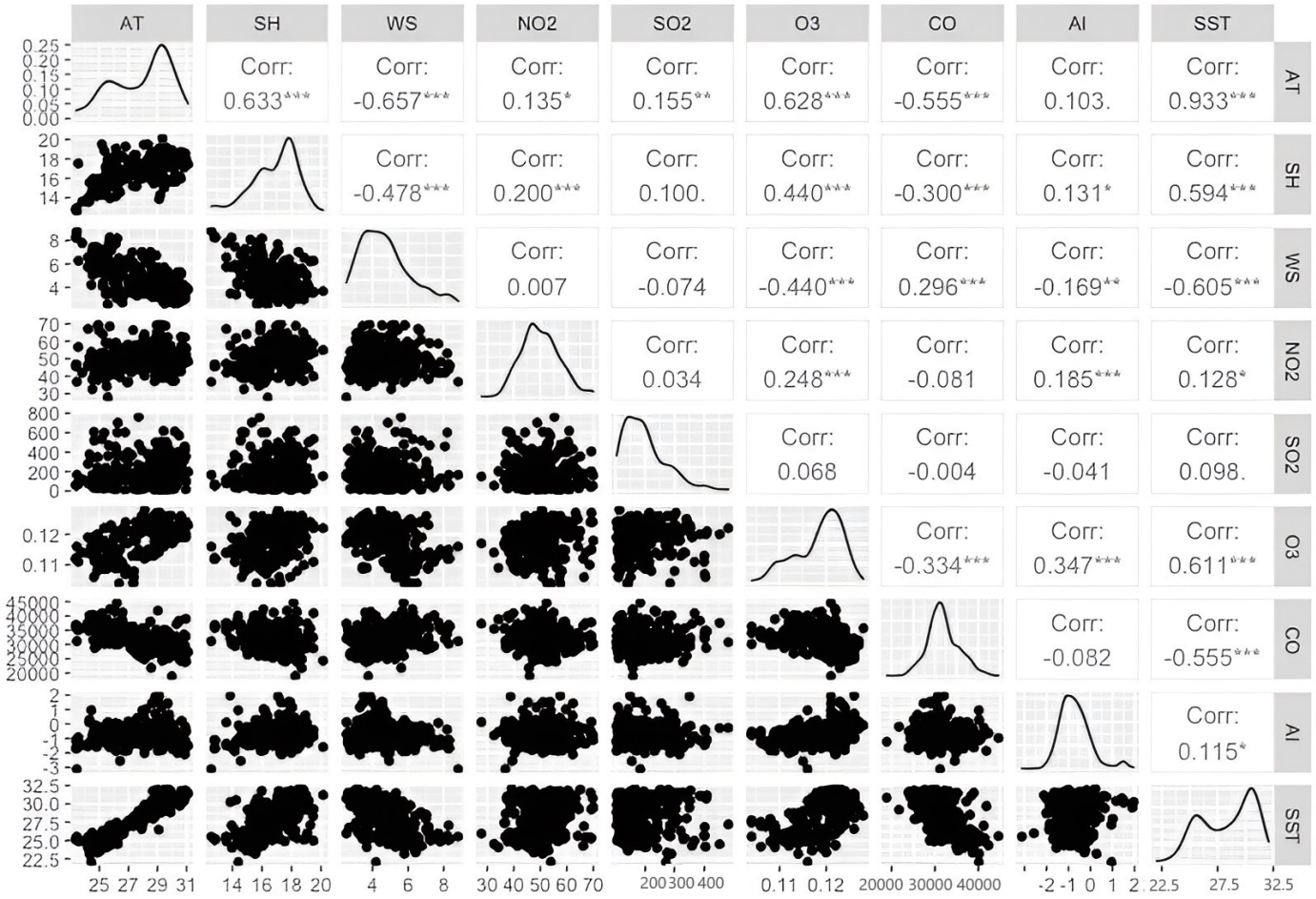

Figure 2. Correlation plot (note: * indicates a 5% significant level, ** indicates a 1% significant level, and *** indicates a 0.1% significant level).

In the left part of Figure 2, the scatter plot indicates the data distribution and its linearity with corresponding variables. NO_2, AI, and CO do not exhibit strong linearity with the rest of the variables. SST and WS show dynamic linearity with their seasonal-changing characteristics. Further, the diagonally presented line plot shows the explicit symmetry of the assessed data. It indicates positive symmetry only for WS and SO_2 and negative for the rest.

3.3. Spatiotemporal Variation in Aerosol Index and Trace Gas Distribution

Figure 3 illustrates the spatiotemporal distribution of atmospheric pollutants over the Red Sea with seasonal variation. Substantial NO_2 vertical tropospheric column concentrations (80–105 $\mu molm^{-2}$) were apparent in the northern and northeastern parts of the Red Sea, particularly at high latitudes (Figure 3a). Further, the seasonal contrast also identifies a high rate of pollution (120 $\mu molm^{-2}$) during autumn (October–November) in the eastern course of the Red Sea near Egypt and the Gulf of Suez. Here, the back trajectories correspondingly show a high concentration of the air masses mentioned in Figure 4. Along with marine transportation, extensive industrial activities and ongoing economic projects near these ports may cause such emissions [57]. An area with a significant high SO_2 column concentration (650–750 $\mu molm^{-2}$) was in the upper altitudes (northern and northeastern courses of the Red Sea) near the Gulf of Suez and Port Sudan (Figure 3b). However, the hotspot shifted slightly to the southeastern course of the Al Hudaydah from July to August (400–600 $\mu molm^{-2}$), with substantial marine transportation origins, significant sulfur emissions, and anthropogenic activities [58].

The figure further demonstrates a higher O_3 column concentration (130 $\mu molm^{-2}$) on the north slope of the Red Sea throughout the whole year near the Egyptian sea course, Port Sudan, and Asmara (Figure 3c). However, Figure 3c (autumn) shows a significant O_3 concentration (127 $\mu molm^{-2}$) in the southern part of Jeddah Port, Saudi Arabia. Hotspots with high CO concentrations (32 $mmolm^{-2}$) can be distinguished all over the Red Sea (Figure 3d). Since the Red Sea is one of the busiest routes for marine transport, a substantial amount of marine fuel burning can be distinguished by its lethal emissions. Moreover, the southwest part of the Red Sea can be marked as a significant hotspot (<38 $mmolm^{-2}$) from December to June. The AI concentration over the Red Sea shows distinctive patterns from July to September (approximate AI ranges near 0.25) in the lower longitude of the Red Sea in Yemen, Eritrea, and Sudan (Figure 3e).

However, a strong AI (0.5–0.75) was detected in nearby land areas all over the Red Sea. Predominantly in the Red Sea, Saharan dust storms from the Arabian Peninsula form tropospheric aerosols, which are more frequent in the summer [59].

3.4. Back Trajectory Analysis

The mean air masses adopted from the "model vertical velocity" reached at multiple locations over the Red Sea in 2019 are visualized in Figure 4. It is apparent from Figure 4a–d that the trajectories with distinct sources have seasonal variation since the Red Sea's water circulation is stimulated by the interaction of velocity, convection, and tides with the overlying atmosphere [60]. The most common back trajectory patterns illustrate a higher concentration of air masses in the long-range northwesterly pattern for July, while the shorter eastward loops of air mass loading are significant for January. The eastward air flow is significant in July because the Northern Hemisphere is inclined toward the sun and receives more sunlight during the day. On the contrary, the aerodynamics are inverted during January because the southern hemisphere obtained more daylight than the northern hemisphere.

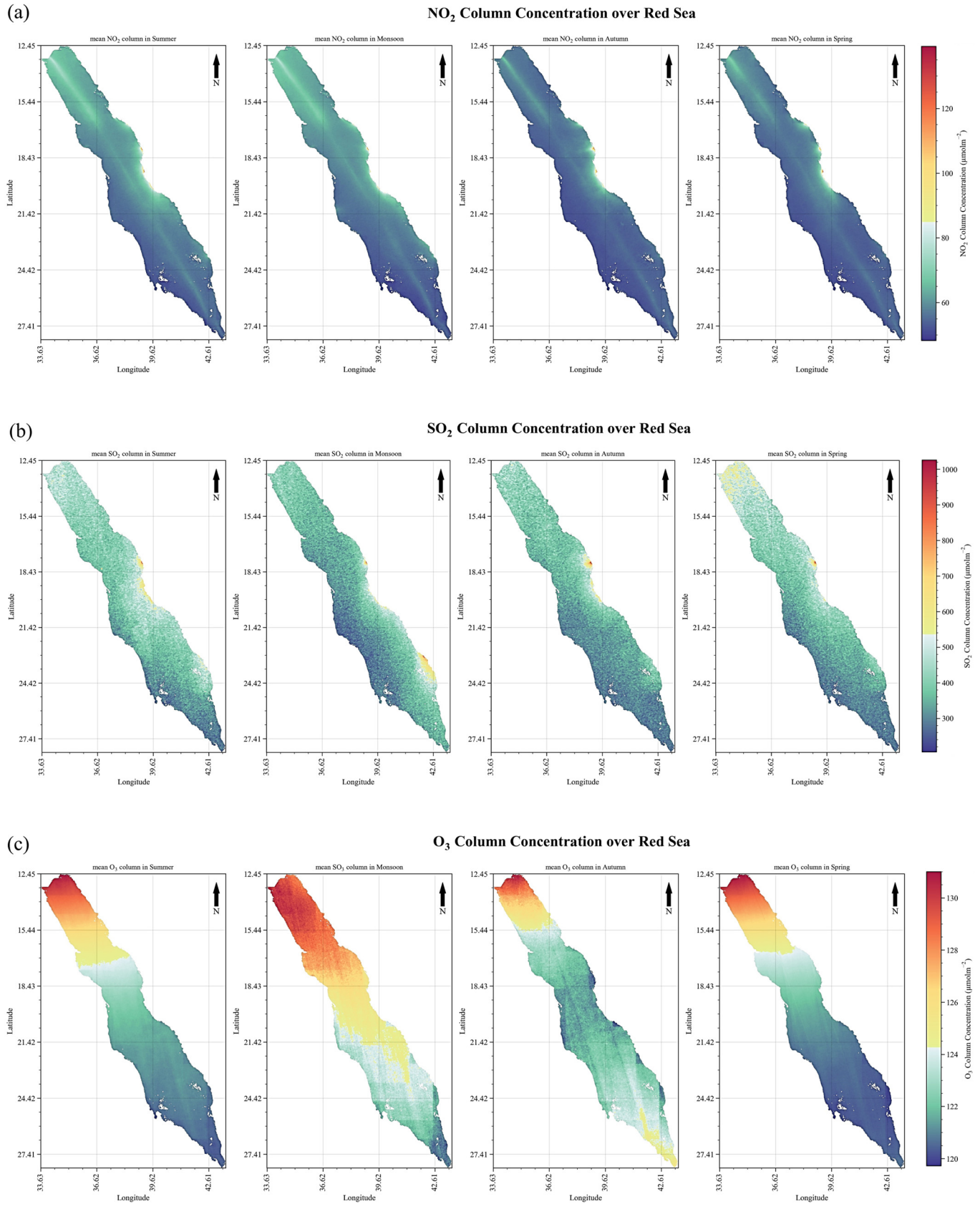

Figure 3. *Cont.*

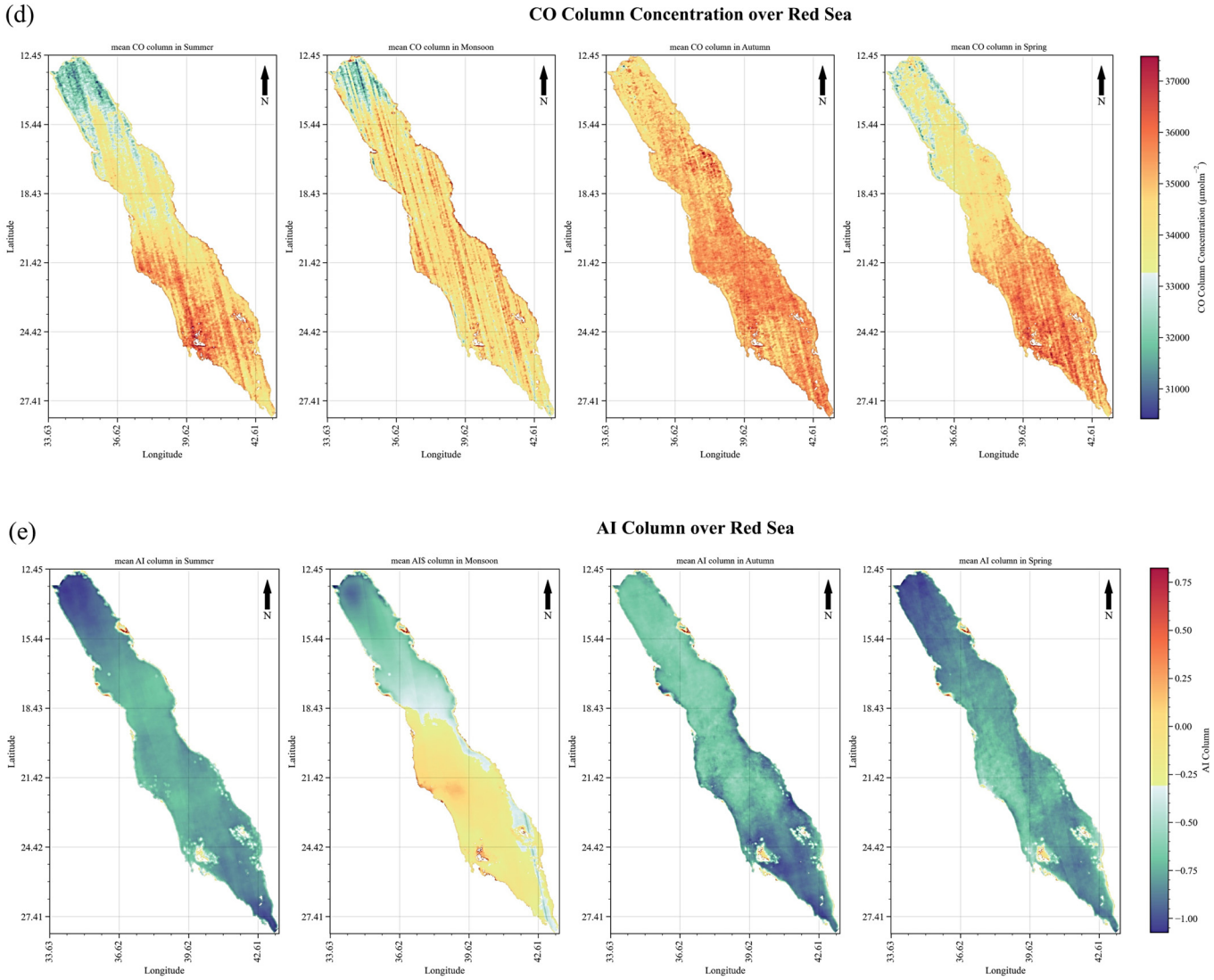

Figure 3. Seasonal averaged (**a**) NO_2, (**b**) SO_2, (**c**) O_3, (**d**) CO, and (**e**) AI columns over the Red Sea in summer (March–June), monsoon (July–August), autumn (September–November), and winter (December–February).

Moreover, seasonal winds blow southeast all year in the northern course of the river (north of 19–20°N). The seasonal vector mean wind fields at 200 hPa exhibit high spatial variability and considerable cross-axis features of the wind components (Figure 5). The images show the wind jets' occurrence and timing by displaying dust plumes sweeping off the coast. The monthly mean wind field shows these wind jets as the westward wind components over the Saudi Arabian coast north of 22N. Eddies are common in the Red Sea all year round, according to satellite altimetry, with the most noticeable pair occurring in July and/or August close to the Tokar Gap around 19N. Still, in the south, the winds start reversing from northwesterly in the warmer months to southeasterly in winter due to the Arabian monsoon [61,62]. Further, the air masses flow in a very similar pattern at 1000 m AGL all over the year, with a significantly long pathway. This implies the subsequent influence of tropical air, moving mass from the subtropical jet stream to the polar jet stream. However, the upper latitude (27.60°N, 34.27°E) of the Red Sea demonstrates northwesterly patterns for all seasons (except Figure 4d), while the lower latitude (12.87°N, 43.22°E) demonstrates southeasterly trajectory simulation only in Figure 4c,d for a higher comparative elevation (2500 m).

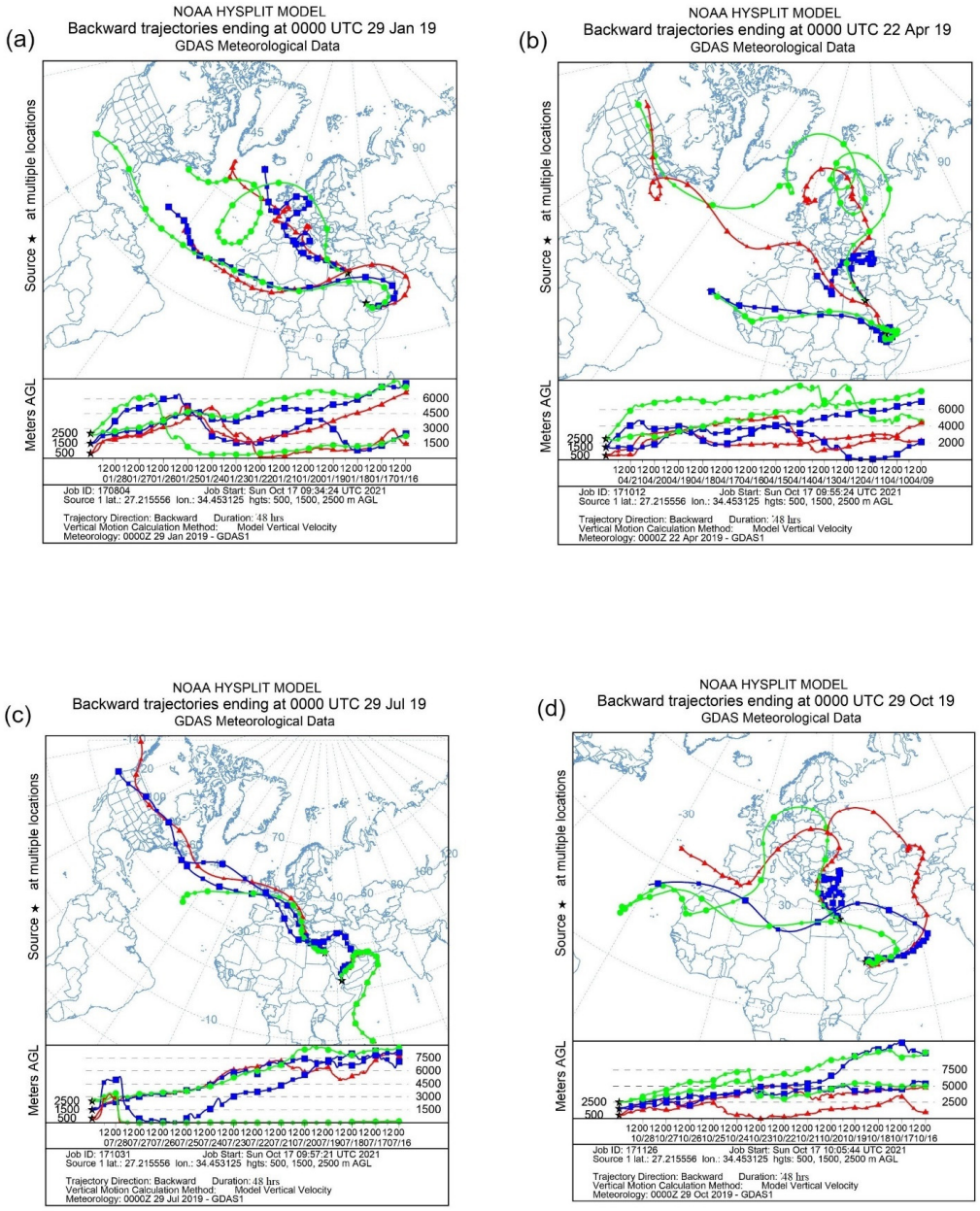

Figure 4. Backward trajectory using the HYPLIT model over the Red Sea level using GDAS 1° × 1° meteorological data classified by 48 h. Here, (**a**) corresponds to the mean backward trajectory in January 2019, (**b**) corresponds to the mean backward trajectory in April 2019, (**c**) corresponds to the mean backward trajectory in July 2019, and (**d**) corresponds to the mean backward trajectory in October 2019 at 500 m (red line), 1500 m (blue line), and 2500 m (green line) above ground. "★" indicating potential pollutant clusters in each pressure level.

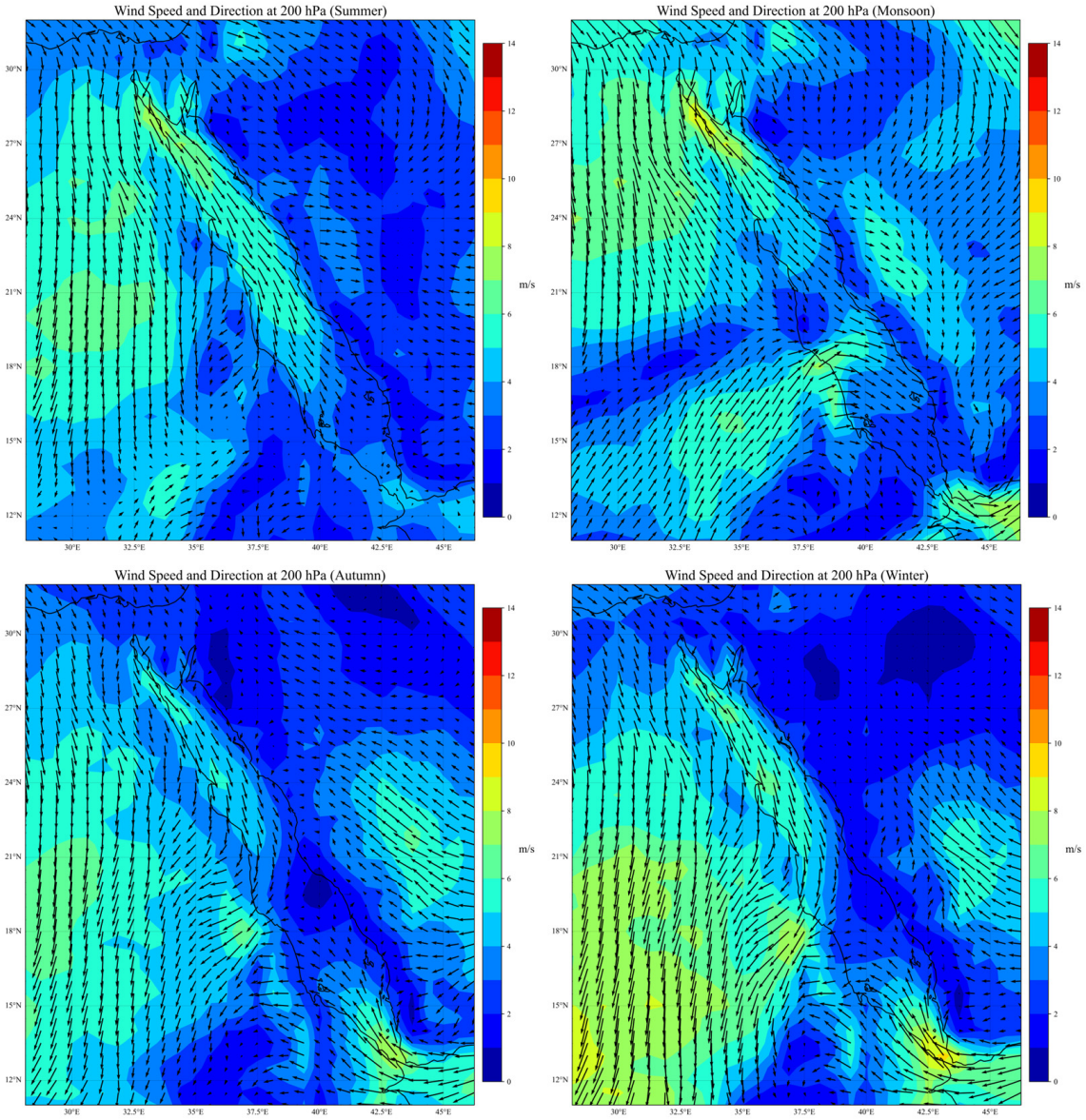

Figure 5. Distribution of seasonal wind vector at 200 hPa over the Red Sea.

3.5. Principal Component Analysis

The results of the PCA loadings after varimax rotation and scree plots of the principal components are shown in Table 3 and Figure 6, respectively. PCA was employed on the selected pollution and meteorological measurements to reduce data dimensions. The examined time-series data resulted in three principal components with eigenvalues greater than 1, explaining 77.3% of the total variance, and factor loading values of more than 50%.

Table 3 shows the eigenvalues and accumulated variance of PCA for both the pollution and meteorological data. In our study, the first principal component (PC1) has an eigenvalue of 3.87 and explains 43% of the variance, which is influenced by all the meteorological parameters (factor loadings > 0.5). While the AT, SST, SH, and O_3 show positive loadings, the WS (−0.753) and CO (−0.650) show strong negative loadings. The contribution of the air and sea surface temperatures to changing the distribution of pollutants is evident, comprising a factor loading greater than 90%. The second component (PC2) has an eigenvalue of 1.21 and explains 13.45% of the total variance. PC2 is significantly influenced by NO_2, O_3, and AI with positive factor loadings. NO_2 shows the highest factor loading, with 75% loading statistics in PC2. The AI and NO_2 are not shown in Table 3 as they comprise lower factor loadings (<0.5). The only contributor in the third component (PC3) is SO_2, with

a factor loading of 0.94. The lower factor loadings of SO_2 in PC1 and PC2 show strong multicollinearity with other selected observations.

Table 3. Principal component analysis of air pollutants and meteorological data.

Variables	PC1	PC2	PC3
Air temperature	0.944	-	-
Sea Surface Temperature	0.925	-	-
Specific Humidity	0.691	-	-
Wind Speed	−0.753	-	-
NO_2	-	0.752	
SO_2	-	-	0.937
O_3	0.652	0.55	-
CO	−0.650	-	-
AI	-	0.739	-
Eigenvalue	3.87	1.21	1.02
Variability (%)	42.97	13.46	11.28
Cumulative (%)	43.0	56.4	77.3

"-" indicates obtained factor loading less than 0.5 for corresponding variables.

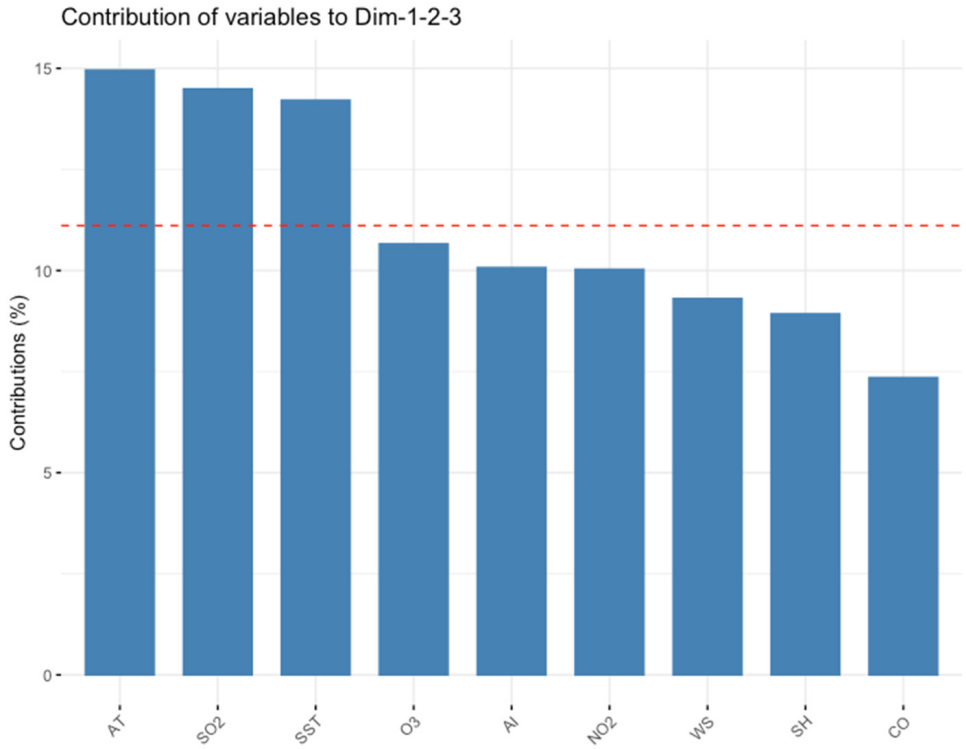

Figure 6. Scree plot of first nine principal components.

4. Discussions

The statistical evidence on pollutant columns and meteorological parameters demonstrates a high level of consistency with minimal deviation from the mean measurements. The data concerning NO_2, SO_2, CO, and the AI exhibit positive skewness, indicating that a greater concentration of the data points lies above the statistical measure of the central tendency. This suggests a continual upward trend in oceanic air pollution. The spatiotemporal distribution illustrates significant NO_2, SO_2, and O_3 hotspots in the northern and northeastern regions. A substantial amount of NO_x and other pollutants often form tropospheric O_3 from a significant chemical reaction [63]. Kerr et al. (2019) [64] also demonstrated a similar relationship between the tropospheric O_3 and jet pressure near the mid-latitudes (30°N). Therefore, poleward air accumulation can be distinguished as contributing to the high

concentration of O_3 on the northern coast. Moreover, the back trajectories also illustrate similar air mass trajectories (Figure 4c) during this period. Further, the CO column shows a significantly high air pollutant concentration zone all over the Red Sea, particularly in the southwestern regions of Yemen, Sudan, and the Gulf of Suez. CO adversely impacts human health [65].

The AI shows a very high fluctuation statistic (with a column mean of -0.699 ± 0.726), which can also be observed in the spatiotemporal distribution of the AI. A significant AI hotspot is found near the southwestern part of the Red Sea. This can be explained as the result of sudden dust storms coming from the North African or Saharan region. It is worth noting that the mean temperature measured by Shaltout [51] in 2016 was a bit lower than our findings. With the increasing AT, the air fluxes gain significant momentum, and thus a post-summer dust storm appears in the Red Sea, blowing near the Tokar Gap. The spatiotemporal distribution of the trace gases and AI shows a significant variation in the yearly averaged data over the Red Sea.

Oceangoing ships are a major contributor to air pollution over the Red Sea. Maritime ships emit NO_x, SO_x, CO, and volatile organic compounds (VOCs) around the coastal regions, including major ports [66]. In PC1, O_3 is positively loaded. O_3 is photochemically formed when its precursors, NO_x (combustion of NO and NO_2), CO, and VOCs, are abundant in sunlight. Anthropogenic emissions of O_3 precursors are considered to be significant sources of net O_3 production [67]. Therefore, the source of precursors could be anthropogenic and biogenic sources of VOCs, NO_x, and CO (from ships, fuel combustion, and industrial activities near the seaports [68]). The presence of high temperatures, intense solar radiation, and anthropogenic NO_x and VOC emissions constitutes a source of tropospheric O_3 over the Red Sea [69]. Moreover, onshore and offshore petrochemical industries, dense maritime traffic, fossil energy production for air conditioning and desalination, and several urban activities are known precursors of O_3. Such actions are expected to intensify further in the future and contribute to photochemical O_3 production [26,63].

Moreover, CO plays a significant role in forming ground-level O_3 [70]. The natural sources of CO are natural gas, oil, and ocean emissions [71]. An anthropogenic source can be considered incomplete combustion from marine transports [72]. Moreover, CO is produced photochemically on the surface of the ocean and emitted into the atmosphere [73]. In PC2, NO_2 is positively loaded. The oceangoing ships and industrial activities near the Red Sea are the primary sources of NO_2 emissions over the Red Sea. In PC2, NO_x is not strongly correlated with O_3, and this could be due to the non-linearity of O_3 formation in the troposphere [74]. Moreover, this non-linearity is strongly linked to the distribution of NO_x sources [7]. The AI measures the presence of UV absorption, like dust and smoke. High values of the AI indicate the increased loading of elevated, absorbing aerosols often seen over desert or biomass-burning regions [75], while negative values indicate non-absorbing aerosol. Sand and dust storms originated in the Arabian Peninsula and are common natural phenomena that carry dust aerosols over long distances from their source [59]. On PC3, only SO_2 is loaded. The primary sources of SO_2 emissions over the Red Sea are maritime oil platforms, oil-powered industries near the Red Sea, and the burned fuel of oceangoing ships. Inconsistent pollution sources and high wind activity may have resulted in the multicollinearity of the SO_2 statistics, and thus no significant relationship was observed between SO_2 and the other parameters.

The adverse impact of air pollution resulting from non-point sources poses a significant threat to the ecological system. The sea-axis alignment of the climatological mean wind within the Red Sea is attributable to the presence of towering mountain ranges encircling the sea (Figure 5). The back trajectories show a significant long-range air mass movement detected in the northeastern part of the Red Sea from Egypt, Libya, Sudan, and Eritrea. Here, the trajectory pattern at 2500 m AGL shows that transported air masses over the Mediterranean Sea are considerable, with a significant response to the subtropical jet stream. For July, the trajectories for similar heights show a higher concentration from the southeastern region, significantly from the Arabian Sea. Here, the high momentum of

the air masses from the equator shrinks near the 30°N latitude and further follows the natural westward wind circulation in the Hadley Cell. Such long-range air mass transport can generate haze, accumulating significant aerosol particles [76,77]. As a result, the jet flux caused distinct air mass circulation. Further, in Figure 4a,b,d, air masses with high latitudes demonstrate loop trajectories heading from the northeast to the northwest to reach a higher latitude at an altitude of 2500 m AGL. Similar trajectory patterns of air masses were also demonstrated by Ramachandran and Jayaraman (2003) [78] while studying the optical depth over the Bay of Bengal. Nevertheless, the air mass at a lower latitude of the Red Sea shows a distinct pattern in Figure 4c, where air mass at an altitude of 500 m transports southeasterly while air mass at 1000 m and 2500 m meanders north–east. Thus, back trajectories indicate distinctive sources regarding the extreme seasonal contrast. The longer the average trajectory of the air masses, the quicker the intensity of the movement.

5. Conclusions

This article focused on assessing spatiotemporal distributions, detecting the trajectory pattern of air pollutants, and examining the influence of meteorological parameters on air pollutants over the Red Sea. Traced pollutants, notably NO_2 (50.1 ± 7.32 $\mu molm^{-2}$), CO ($31{,}905 \pm 3701$ $\mu molm^{-2}$), and O_3 (0.118 ± 0.005 $\mu molm^{-2}$), show high mean vertical tropospheric column concentrations in coastal environments. All the selected meteorological parameters significantly correlate positively with the pollutants, though the WS shows a significant negative correlation. The spatial variation in air pollutants and the AI observed over the Red Sea illustrates the significant seasonal variation in the northeastern course. Again, from the back trajectory analysis, the source illustrates a substantial northwesterly air mass trajectory and a westward loop in the northern course of the Red Sea. Here, air masses flow in the Hadley Cell, transporting significant pollutants to the northern coast. Therefore, the trajectory indicates potential anthropogenic sources transported over a long distance and with significant influence from the wind. These hotspots of air pollutants can be indicated as high environmental deterioration zones. The PCA suggests a relationship between the meteorological data and CO and O_3. The levels of NO_2, O_3, and AI changed in similar ways. Anthropogenic sources can be attributed as the primary sources of this pollutant emission in this region. The influence of meteorological parameters is also significant. Therefore, the PCA supports our understanding of the influence of meteorological parameters on air pollution over the Red Sea.

Moving forward, future research in the study of air quality dynamics over the Red Sea could benefit from employing advanced methodologies beyond correlation analyses to unravel complex cause–effect relationships. Potential avenues for future exploration involve the integration of techniques such as Granger causality, time series analysis, and spatial modeling [79,80]. These methodologies can shed light on causal connections between diverse environmental and meteorological variables impacting air quality. Additionally, combining these approaches with the back trajectory methodology could elucidate the influence of various regions on each other, providing insights into the transportation of air masses and pollutants across the Red Sea. Furthermore, employing time-dependent correlations may facilitate the identification of characteristic time delays between different quantities and regions, unveiling temporal patterns and relationships. By adopting a multifaceted approach encompassing causal analysis from both temporal and spatial dimensions and exploring characteristic time delays, future studies can aim to advance our understanding of the intricate interplay among factors influencing air quality dynamics in the Red Sea region.

Author Contributions: Conceptualization, B.M., A.-E.E.H. and S.M.R.; methodology, K.M., M.S.U. and N.D.; software, S.K.N., A.-E.E.H. and A.T.; validation, S.K.N., A.-E.E.H. and A.T.; formal analysis, B.M., M.S. and K.M.; resources, M.M.R. and S.M.R.; data curation, B.M. and A.T.; writing—original draft preparation, B.M., A.-E.E.H. and K.M.; writing—review and editing, B.M., M.S., S.M.R. and M.M.R.; visualization, A.-E.E.H. and K.M.; supervision, S.M.R. and M.M.R.; project administration, S.M.R. and M.M.R.; funding acquisition, M.M.R. All authors have read and agreed to the published version of the manuscript.

Funding: This work was supported by the Deanship of Scientific Research, Vice Presidency for Graduate Studies and Scientific Research, King Faisal University, Saudi Arabia (Grant No. 3133).

Data Availability Statement: The data that support the findings of this study are available from the corresponding author, Muhammad Muhitur Rahman (mrahman@kfu.edu.sa), or the first author, Bijoy Mitra (bijoymitra11@gmail.com), upon reasonable request.

Acknowledgments: The authors acknowledge the support received from King Faisal University (KFU) and King Fahd University of Petroleum & Minerals (KFUPM), Saudi Arabia.

Conflicts of Interest: The authors declare no conflicts of interest.

References

1. Liu, H.; Jin, X.; Wu, L.; Wang, X.; Fu, M.; Lv, Z.; Morawska, L.; Huang, F.; He, K. The impact of marine shipping and its DECA control on air quality in the Pearl River Delta, China. *Sci. Total Environ.* **2018**, *625*, 1476–1485. [CrossRef]
2. Han, S.; Cai, Z.; Liu, J.; Zhang, M.; Chen, J.; Lin, Y. Comparison on aerosol physicochemical properties of sea and land along the coast of Bohai, China. *Sci. Total Environ.* **2019**, *673*, 148–156. [CrossRef]
3. Corbett, J.J.; Fischbeck, P.S.; Pandis, S.N. Global nitrogen and sulfur inventories for oceangoing ships. *J. Geophys. Res. Atmos.* **1999**, *104*, 3457–3470. [CrossRef]
4. IMO. *Fourth IMO GHG Study 2020 Executive Summary*; The Convention on the International Maritime Organization: London, UK, 2020.
5. Ledoux, F.; Roche, C.; Cazier, F.; Beaugard, C.; Courcot, D. Influence of ship emissions on NO_x, SO_2, O_3 and PM concentrations in a North-Sea harbor in France. *J. Environ. Sci.* **2018**, *71*, 56–66. [CrossRef] [PubMed]
6. Viana, M.; Hammingh, P.; Colette, A.; Querol, X.; Degraeuwe, B.; de Vlieger, I.; van Aardenne, J. Impact of maritime transport emissions on coastal air quality in Europe. *Atmos. Environ.* **2014**, *90*, 96–105. [CrossRef]
7. Endresen, Ø.; Sørgård Det Norske Veritas, E.; Jostein Sundet, N.K.; Dalsøren, S.B.; Isaksen, I.S.A.; Berglen, T.F.; Norske Veritas, D. Emission from International Sea Transportation and Environmental Impact. *J. Geophys. Res.* **2003**, *108*, 4560. [CrossRef]
8. Eyring, V.; Isaksen, I.S.; Berntsen, T.; Collins, W.J.; Corbett, J.J.; Endresen, O.; Grainger, R.G.; Moldanova, J.; Schlager, H.; Stevenson, D.S. Transport impacts on atmosphere and climate: Shipping. *Atmos. Environ.* **2010**, *44*, 4735–4771. [CrossRef]
9. Eyring, V.; Köhler, H.W.; Van Aardenne, J.; Lauer, A. Emissions from International Shipping: 1. The Last 50 Years. *J. Geophys. Res. D Atmos.* **2005**, *110*, 171–182. [CrossRef]
10. Walker, D.I.; Ormond, R.F.G. Coral death from sewage and phosphate pollution at Aqaba, Red Sea. *Mar. Pollut. Bull.* **1982**, *13*, 21–25. [CrossRef]
11. Khatib, H. Oil and natural gas prospects: Middle East and North Africa. *Energy Policy* **2014**, *64*, 71–77. [CrossRef]
12. Dalsøren, S.B.; Endresen, Ø.; Isaksen, I.S.A.; Gravir, G.; Sörgärd, E. Environmental Impacts of the Expected Increase in Sea Transportation, with a Particular Focus on Oil and Gas Scenarios for Norway and Northwest Russia. *J. Geophys. Res. Atmos.* **2007**, *112*. [CrossRef]
13. Endresen, Ø.; Sørgård, E.; Behrens, H.L.; Brett, P.O.; Isaksen, I.S.A. A Historical Reconstruction of Ships' Fuel Consumption and Emissions. *J. Geophys. Res. Atmos.* **2007**, *112*. [CrossRef]
14. Lawrence, M.G.; Crutzen, P.J. Influence of NO_x emissions from ships on tropospheric photochemistry and climate. *Nature* **1999**, *402*, 167–170. [CrossRef]
15. Agulles, M.; Jordà, G.; Jones, B.; Agustí, S.; Duarte, C.C. Temporal evolution of temperatures in the red sea and the gulf of aden based on in situ observations (1958–2017). *Ocean Sci.* **2020**, *16*, 149–166. [CrossRef]
16. Karnauskas, K.B.; Jones, B.H. The Interannual Variability of Sea Surface Temperature in the Red Sea From 35 Years of Satellite and In Situ Observations. *J. Geophys. Res. Ocean* **2018**, *123*, 5824–5841. [CrossRef]
17. Richter, A.; Eyring, V.; Burrows, J.P.; Bovensmann, H.; Lauer, A.; Sierk, B.; Crutzen, P.J. Satellite Measurements of NO_2 from International Shipping Emissions. *Geophys. Res. Lett.* **2004**, *31*, 1–4. [CrossRef]
18. Seddiek, I.S.; Elgohary, M.M. Eco-Friendly Selection of Ship Emissions Reduction Strategies with Emphasis on SO_x and NO_x Emissions. *Int. J. Nav. Archit. Ocean Eng.* **2014**, *6*, 737–748. [CrossRef]
19. Alahmadi, S.; Al-Ahmadi, K.; Almeshari, M. Spatial Variation in the Association between NO_2 Concentrations and Shipping Emissions in the Red Sea. *Sci. Total Environ.* **2019**, *676*, 131–143. [CrossRef]
20. Hu, M.; Wang, Y.; Wang, S.; Jiao, M.; Huang, G.; Xia, B. Spatial-Temporal Heterogeneity of Air Pollution and Its Relationship with Meteorological Factors in the Pearl River Delta, China. *Atmos. Environ.* **2021**, *254*, 118415. [CrossRef]

21. Tyagi, B.; Singh, J.; Beig, G. Seasonal Progression of Surface Ozone and NO_x Concentrations over Three Tropical Stations in North-East India. *Environ. Pollut.* **2020**, *258*, 113662. [CrossRef]
22. Bourtsoukidis, E.; Pozzer, A.; Sattler, T.; Matthaios, V.N.; Ernle, L.; Edtbauer, A.; Fischer, H.; Könemann, T.; Osipov, S.; Paris, J.D.; et al. The Red Sea Deep Water Is a Potent Source of Atmospheric Ethane and Propane. *Nat. Commun.* **2020**, *11*, 447. [CrossRef]
23. Pedgley, D.E. An Outline of the Weather and Climate of the Red Sea. *L'oceanographie Phys. Mer Rouge* **1974**, *11*, 9–27.
24. Jiang, H.; Farrar, J.T.; Beardsley, R.C.; Chen, R.; Chen, C. Zonal Surface Wind Jets across the Red Sea Due to Mountain Gap Forcing along Both Sides of the Red Sea. *Geophys. Res. Lett.* **2009**, *36*. [CrossRef]
25. Held, I.; Hou, A. Nonlinear Axially Symmetric Circulations in a Nearly Inviscid Atmosphere. *J. Atmos. Sci.* **1980**, *37*, 515–533. [CrossRef]
26. Tadic, I.; Crowley, J.N.; Dienhart, D.; Eger, P.; Harder, H.; Hottmann, B.; Martinez, M.; Parchatka, U.; Pari, J.D.; Pozzer, A.; et al. Net Ozone Production and Its Re-lationship to Nitrogen Oxides and Volatile Organic Compounds in the Marine Boundary Layer around the Arabian Pen-insula. *Atmos. Chem. Phys.* **2020**, *20*, 6769–6787. [CrossRef]
27. Veefkind, J.P.; Aben, I.; McMullan, K.; Förster, H.; de Vries, J.; Otter, G.; Claas, J.; Eskes, H.J.; de Haan, J.F.; Kleipool, Q.; et al. TROPOMI on the ESA Sentinel-5 Precursor: A GMES Mission for Global Observations of the Atmospheric Composition for Climate, Air Quality and Ozone Layer Applications. *Remote Sens. Environ.* **2012**, *120*, 70–83. [CrossRef]
28. Sun, J.; Gong, J.; Zhou, J. Estimating Hourly PM2.5 Concentrations in Beijing with Satellite Aerosol Optical Depth and a Random Forest Approach. *Sci. Total Environ.* **2021**, *762*, 144502. [CrossRef]
29. Tabunschik, V.; Gorbunov, R.; Gorbunova, T. Unveiling Air Pollution in Crimean Mountain Rivers: Analysis of Sentinel-5 Satellite Images Using Google Earth Engine (GEE). *Remote Sens.* **2023**, *15*, 3364. [CrossRef]
30. Bosworth, W.; Huchon, P.; McClay, K. The Red Sea and Gulf of Aden Basins. *J. Afr. Earth Sci.* **2005**, *43*, 334–378. [CrossRef]
31. Loya, Y. Recolonization of Red Sea Corals Affected by Natural Catastrophes and Man-Made Perturbations. *Ecology* **1976**, *57*, 278–289. [CrossRef]
32. Rozanov, V.V.; Diebel, D.; Spurr, R.J.D.; Burrows, J.P. GOMETRAN: A Radiative Transfer Model for the Satellite Project GOME, the Plane-Parallel Version. *J. Geophys. Res. Atmos.* **1997**, *102*, 16683–16695. [CrossRef]
33. Galli, A.; Butz, A.; Scheepmaker, R.A.; Hasekamp, O.; Landgraf, J.; Tol, P.; Wunch, D.; Deutscher, N.M.; Toon, G.C.; Wennberg, P.O.; et al. CH_4, CO, and H_2O Spectroscopy for the Sentinel-5 Precursor Mission: An As-sessment with the Total Carbon Column Observing Network Measurements. *Atmos. Meas. Tech.* **2012**, *5*, 1387–1398. [CrossRef]
34. Irizar, J.; Melf, M.; Bartsch, P.; Koehler, J.; Weiss, S.; Greinacher, R.; Erdmann, M.; Kirschner, V.; Perez Albinana, A.; Martin, D. Sentinel-5/UVNS. In Proceedings of the International Conference on Space Optics—ICSO 2018, Chania, Greece, 9–12 October 2018; SPIE: Bellingham, WA, USA, 2019; pp. 41–58. [CrossRef]
35. Stratoulias, D.; Nuthammachot, N. Air Quality Development during the COVID-19 Pandemic over a Medium-Sized Urban Area in Thailand. *Sci. Total Environ.* **2020**, *746*, 141320. [CrossRef] [PubMed]
36. Ogen, Y. Assessing Nitrogen Dioxide (NO_2) Levels as a Contributing Factor to Coronavirus (COVID-19) Fatality. *Sci. Total Environ.* **2020**, *726*, 138605. [CrossRef] [PubMed]
37. Zhao, F.; Liu, C.; Cai, Z.; Liu, X.; Bak, J.; Kim, J.; Hu, Q.; Xia, C.; Zhang, C.; Sun, Y.; et al. Ozone Profile Retrievals from TROPOMI: Implication for the Variation of Tropospheric Ozone during the Outbreak of COVID-19 in China. *Sci. Total Environ.* **2021**, *764*, 142886. [CrossRef]
38. Hashim, B.M.; Al-Naseri, S.K.; Al-Maliki, A.; Al-Ansari, N. Impact of COVID-19 Lockdown on NO_2, O_3, PM2.5 and PM10 Concentrations and Assessing Air Quality Changes in Baghdad, Iraq. *Sci. Total Environ.* **2021**, *754*, 141978. [CrossRef]
39. Mahmud, K.; Mitra, B.; Uddin, M.S.; Hridoy, A.-E.E.; Aina, Y.A.; Abubakar, I.R.; Rahman, S.M.; Tan, M.L.; Rahman, M.M. Temporal Assessment of Air Quality in Major Cities in Nigeria Using Satellite Data. *Atmos. Environ. X* **2023**, *20*, 100227. [CrossRef]
40. Gujarati, D.; Porter, D.; Gunasekar, S. The McGraw-Hill Series Economics. 2009. Available online: www.downloadslide.com (accessed on 22 April 2021).
41. Benesty, J.; Chen, J.; Huang, Y.; Cohen, I. Pearson Correlation Coefficient. In *Springer Topics in Signal Processing*; Springer Science and Business Media B.V.: Berlin/Heidelberg, Germany, 2009; Volume 2, pp. 1–4. [CrossRef]
42. Stein, A.F.; Draxler, R.R.; Rolph, G.D.; Stunder, B.J.B.; Cohen, M.D.; Ngan, F. NOAA's HYSPLIT Atmospheric Transport and Dispersion Modeling System. *Bull. Am. Meteorol. Soc.* **2015**, *96*, 2059–2077. [CrossRef]
43. Rolph, G.; Stein, A.; Stunder, B. Real-Time Environmental Applications and Display SYstem: READY. *Environ. Mod-Elling Softw.* **2017**, *95*, 210–228. [CrossRef]
44. Su, L.; Yuan, Z.; Fung, J.C.H.; Lau, A.K.H. A Comparison of HYSPLIT Backward Trajectories Generated from Two GDAS Datasets. *Sci. Total Environ.* **2015**, *506–507*, 527–537. [CrossRef]
45. Du, X.; Jin, X.; Zucker, N.; Kennedy, R.; Urpelainen, J. Transboundary Air Pollution from Coal-Fired Power Generation. *J. Environ. Manag.* **2020**, *270*, 110862. [CrossRef] [PubMed]
46. Tian, J.; Fang, C.; Qiu, J.; Wang, J. Analysis of Pollution Characteristics and Influencing Factors of Main Pollutants in the Atmosphere of Shenyang City. *Atmosphere* **2020**, *11*, 766. [CrossRef]
47. Iarocci, G.; Cocchiara, R.A.; Sestili, C.; Del Cimmuto, A.; La Torre, G. Variation of Atmospheric Emissions within the Road Transport Sector in Italy between 1990 and 2016. *Sci. Total Environ.* **2019**, *692*, 1276–1281. [CrossRef]
48. Pio, C.A.; Nunes, T.V.; Borrego, C.S.; Martins, J.G. Assessment of Air Pollution Sources in an Industrial Atmosphere Using Principal Component and Multilinear Regression Analysis. *Sci. Total Environ.* **1989**, *80*, 279–292. [CrossRef]

49. Dominick, D.; Juahir, H.; Latif, M.T.; Zain, S.M.; Aris, A.Z. Spatial Assessment of Air Quality Patterns in Malaysia Using Multivariate Analysis. *Atmos. Environ.* **2012**, *60*, 172–181. [CrossRef]
50. Lever, J.; Krzywinski, M.; Altman, N. Principal component analysis. *Nature* **2017**, *14*, 641–642. [CrossRef]
51. Shaltout, M. Recent Sea Surface Temperature Trends and Future Scenarios for the Red Sea. *Oceanologia* **2019**, *61*, 484–504. [CrossRef]
52. Myriokefalitakis, S.; Daskalakis, N.; Fanourgakis, G.S.; Voulgarakis, A.; Krol, M.C.; Aan de Brugh, J.M.J.; Kanakidou, M. Ozone and Carbon Monoxide Budgets over the Eastern Mediterranean. *Sci. Total Environ.* **2016**, *563–564*, 40–52. [CrossRef]
53. Wu, Y.; Liu, D.; Wang, X.; Li, S.; Zhang, J.; Qiu, H.; Ding, S.; Hu, K.; Li, W.; Tian, P.; et al. Ambient Marine Shipping Emissions Determined by Vessel Operation Mode along the East China Sea. *Sci. Total Environ.* **2021**, *769*, 144713. [CrossRef]
54. Islam, M.S.; Rahman, M.; Tusher, T.R.; Roy, S.; Razi, M.A. Assessing the Relationship between COVID-19, Air Quality, and Meteorological Variables: A Case Study of Dhaka City in Bangladesh. *Aerosol Air Qual. Res.* **2021**, *21*, 200609. [CrossRef]
55. Banta, R.M.; Senff, C.J.; Alvarez, R.J.; Langford, A.O.; Parrish, D.D.; Trainer, M.K.; Darby, L.S.; Michael Hardesty, R.; Lambeth, B.; Andrew Neuman, J.; et al. Dependence of Daily Peak O_3 Concentrations near Houston, Texas on Environmental Factors: Wind Speed, Temperature, and Boundary-Layer Depth. *Atmos. Environ.* **2011**, *45*, 162–173. [CrossRef]
56. Kalbarczyk, R.; Sobolewski, R.; Kalbarczyk, E. Biometeorological Determinants of the Tropospheric Ozone Concentration in the Suburban Conditions of Wroclaw, Poland. *J. Elem.* **2016**, *21*, 729–744. [CrossRef]
57. Abera, A.; Malmqvist, E.; Mandakh, Y.; Flanagan, E.; Jerrett, M.; Gebrie, G.S.; Bayih, A.G.; Aseffa, A.; Isaxon, C.; Mattisson, K. Measurements of NO_x and Development of Land Use Regression Models in an East-African City. *Atmosphere* **2021**, *12*, 519. [CrossRef]
58. Sofiev, M.; Winebrake, J.J.; Johansson, L.; Carr, E.W.; Prank, M.; Soares, J.; Vira, J.; Kouznetsov, R.; Jalkanen, J.P.; Corbett, J.J. Cleaner Fuels for Ships Provide Public Health Benefits with Climate Tradeoffs. *Nat. Commun.* **2018**, *9*, 406. [CrossRef] [PubMed]
59. Jish Prakash, P.; Stenchikov, G.; Kalenderski, S.; Osipov, S.; Bangalath, H. The Impact of Dust Storms on the Arabian Pen-insula and the Red Sea. *Atmos. Chem. Phys.* **2015**, *15*, 199–222. [CrossRef]
60. Bower, A.S.; Farrar, J.T. *Air–Sea Interaction and Horizontal Circulation in the Red Sea*; Springer Earth System Sciences; Springer: Berlin/Heidelberg, Germany, 2015. [CrossRef]
61. Patzert, W.C. Wind-Induced Reversal in Red Sea Circulation. *Deep Sea Res. Oceanogr. Abstr.* **1974**, *21*, 109–121. [CrossRef]
62. Sofianos, S.S.; Johns, W.E. An Oceanic General Circulation Model (OGCM) Investigation of the Red Sea Circulation: 2. Three-Dimensional Circulation in the Red Sea. *J. Geophys. Res. Ocean* **2003**, *108*, 3066. [CrossRef]
63. Pfannerstill, E.Y.; Wang, N.; Edtbauer, A.; Bourtsoukidis, E.; Crowley, J.N.; Dienhart, D.; Eger, P.G.; Ernle, L.; Fischer, H.; Hottmann, B.; et al. Shipborne Measurements of Total OH Reactivity around the Arabian Peninsula and Its Role in Ozone Chemistry. *Atmos. Chem. Phys.* **2019**, *19*, 11501–11523. [CrossRef]
64. Kerr, G.H.; Waugh, D.W.; Strode, S.A.; Steenrod, S.D.; Oman, L.D.; Strahan, S.E. Disentangling the Drivers of the Summertime Ozone-Temperature Relationship Over the United States. *J. Geophys. Res. Atmos.* **2019**, *124*, 10503–10524. [CrossRef]
65. Corbett, J.J.; Fischbeck, P. Emissions from Ships. *Science* **1997**, *278*, 823–824. [CrossRef]
66. Corbett, J.J. Updated Emissions from Ocean Shipping. *J. Geophys. Res.* **2003**, *108*. [CrossRef]
67. Bozem, H.; Butler, T.M.; Lawrence, M.G.; Harder, H.; Martinez, M.; Kubistin, D.; Lelieveld, J.; Fischer, H. Chemical Processes Related to Net Ozone Tendencies in the Free Troposphere. *Atmos. Chem. Phys.* **2017**, *17*, 10565–10582. [CrossRef]
68. Williams, E.J.; Lerrier, B.M.; Murphy, P.C.; Herndon, S.C.; Zahniser, M.S. Emissions of NO_x, SO_2, CO, and HCHO from Commercial Marine Shipping during Texas Air Quality Study (TexAQS) 2006. *J. Geophys. Res. Atmos.* **2009**, *114*, 21306. [CrossRef]
69. Klonecki, A.; Levy, H. Tropospheric chemical ozone tendencies in CO-CH_4-NOy-H_2O system: Their sensitivity to variations in environmental parameters and their application to a global chemistry transport model study. *J. Geophys. Res. Atmos.* **1997**, *102*, 21221–21237. [CrossRef]
70. Mohan, S.; Saranya, P. Assessment of Tropospheric Ozone at an Industrial Site of Chennai Megacity. *J. Air Waste Manag. Assoc.* **2019**, *69*, 1079–1095. [CrossRef] [PubMed]
71. Swinnerton, J.W.; Linnenbom, V.J.; Lamontagne, R.A. The Ocean: A Natural Source of Carbon Monoxide. *Science* **1970**, *167*, 984–986. [CrossRef] [PubMed]
72. Robbins, R.C.; Borg, K.M.; Robinson, E. Carbon Monoxide in the Atmosphere. *J. Air Pollut. Control Assoc.* **1968**, *18*, 106–110. [CrossRef]
73. Bates, T.S.; Kelly, K.C.; Johnson, J.E.; Gammon, R.H. Regional and Seasonal Variations in the Flux of Oceanic Carbon Monoxide to the Atmosphere. *J. Geophys. Res.* **1995**, *100*, 23093–23101. [CrossRef]
74. Isaksen, I.S.A.; Hov, Ø.; Hesstvedt, E. Ozone Generation over Rural Areas. *Environ. Sci. Technol.* **1978**, *12*, 1279–1284. [CrossRef]
75. Soni, M.; Verma, S.; Jethava, H.; Payra, S.; Lamsal, L.; Gupta, P.; Singh, J. Impact of COVID-19 on the Air Quality over China and India Using Long-Term (2009–2020) Multi-Satellite Data. *Aerosol Air Qual. Res.* **2021**, *21*, 200295. [CrossRef]
76. Hanafi, N.H.; Hassim, M.H.; Noor, Z.Z.; Ng, D.K.S.; Harrin Nor Helmi, N.; Aris, N.M. Analysis of Transported Pollution and Haze-Related Diseases via HYSPLIT Trajectory Modelling in the Urbanized Area of Johor, Malaysia. *IOP Conf. Ser. Earth Environ. Sci.* **2019**, *373*, 012008. [CrossRef]
77. Zhai, P.; Bower, A. The Response of the Red Sea to a Strong Wind Jet near the Tokar Gap in Summer. *J. Geophys. Res. Oceans* **2013**, *118*, 421–434. [CrossRef]

78. Ramachandran, S.; Jayaraman, A. Spectral Aerosol Optical Depths over Bay of Bengal and Chennai: II—Sources, Anthro-pogenic Influence and Model Estimates. *Atmos. Environ.* **2003**, *37*, 1951–1962. [CrossRef]
79. Yuan, N.; Fu, Z. Different Spatial Cross-Correlation Patterns of Temperature Records over China: A DCCA Study on Dif-ferent Time Scales. *Phys. A Stat. Mech. Its Appl.* **2014**, *400*, 71–79. [CrossRef]
80. Charakopoulos, A.K.; Katsouli, G.A.; Karakasidis, T.E. Dynamics and Causalities of Atmospheric and Oceanic Data Identified by Complex Networks and Granger Causality Analysis. *Phys. A Stat. Mech. Its Appl.* **2018**, *495*, 436–453. [CrossRef]